Available online at www.sciencedirect.com
ScienceDirect
Trans. Nonferrous Met. Soc. China 26(2016) 2800−2809
Transactions of Nonferrous Metals Society of China
www.tnmsc.cn

Localized dissolution initiated at single and clustered intermetallic particles during immersion of Al−Cu−Mg alloy in sodium chloride solution

Chen LUO[1], Xiaorong ZHOU[2], George E. THOMPSON[2]

1. Aviation Key Laboratory of Science and Technology on Advanced Corrosion and Protection for Aviation Materials, AVIC Beijing Institute of Aeronautical Materials, Beijing 100095, China;
2. School of Materials, The University of Manchester, Manchester M13 9PL, UK

Received 16 August 2015; accepted 18 September 2016

Abstract: Aiming at understanding how intermetallic phases response when AA2024-T3 aluminium alloy is exposed to chloride-containing aqueous medium, scanning electron microscopy was employed to provide morphological information on alloy surface before and after corrosion testing. Energy dispersive X-ray spectroscopy was carried out to determine compositional change in intermetallic particles. Atomic force microscopy was used to examine topographical variation introduced by the reactions of intermetallic phases. Transmission electron microscopy combined with ultramicrotomy was carried out on dealloyed Al_2CuMg particles and their periphery region. It is found that dealloyed Al_2CuMg particles exhibited porous, polycrystalline structure comprised of body-centred cubic copper particles with sizes of 5 to 20 nm. Aluminium matrix started to trench in the periphery of Al_2CuMg particles at the early stage of dealloying. Development of trenching in Al−Cu−Fe−Mn−(Si) particle's periphery was not uniform and took longer time to initiate than Al_2CuMg dealloying. Localized corrosion at a cluster of Al_2CuMg and Al_2Cu particles was mainly associated with Al_2CuMg particles.

Key words: aluminium alloy; intermetallic particle; localized dissolution; dealloying; trenching

1 Introduction

High-strength aluminium alloys such as AA2024-T3 have been widely used for aerospace applications because of their light mass, high strength and damage tolerance [1,2]. Good mechanical properties of these alloys are obtained mainly through nano-sized hardening precipitates, and to a less extent submicron sized dispersoids and coarse intermetallic particles, formed by alloying additions [3,4]. Research has shown that their great corrosion susceptibility is due to the heterogeneous distribution of copper in the alloys, specifically, in the form of copper-rich intermetallic particles [5−7]. Local microgalvanic coupling is established between the inhomogeneities and aluminium matrix and essentially causes localized attack [8−13].

Coarse intermetallic particles interdendritically solidify as lacy networks surrounding the cast grains by the eutectic decomposition. Subsequent ingot homogenization dissolves soluble constituents [14−16]. The remaining particles fracture and become aligned in the direction of metal flow during fabrication of the cast ingots [17]. Copper and other elements, such as iron, manganese and silicon, form intermetallic phases, most of which are cathodic with respect to aluminium. The formation of trenching next to cathodic intermetallic particles in AA2024-T3 aluminium alloy has been well documented [10−13]. LEBLANC and FRANKEL [10] investigated the electrochemical interactions between intermetallic particles and aluminium matrix. The alloy surface was covered by ink before corrosion testing and then scratched using a tip on atomic force microscopy (AFM) cantilever during immersion. No attack was seen in a small exposed area that contained only aluminium matrix or only α-phase (Al−Cu−Fe−Mn−(Si)) particle. Matrix dissolution took place in an area containing a large area fraction of Al−Cu−Fe−Mn particles. Further, Al−Cu−Fe−Mn particles promote oxygen reduction and OH^- generation which consequently results in the

Foundation item: Project (51201157) supported by the National Natural Science Foundation of China; Project (H052013A003) supported by the National Defense Technology Foundation, China; Project supported by the UK-ESPRC LATEST2 Program
Corresponding author: Chen LUO; Tel: +86-13611077600; E-mail: chen.luo.23@qq.com
DOI: 10.1016/S1003-6326(16)64408-4

alkalization of local environment. The electrochemical response of intermetallic phase is heavily dependent on pH. According to BIRBILIS and BUCHHEIT [11], cathodic efficiency of Fe-rich intermetallic phase increased as the pH increased. Thus, it can be predicted that Al−Cu−Fe−Mn particles become more cathodic after corrosion has taken place around them. BUCHLER et al [12] monitored the initiation of those localized corrosion sites that are related to cathodic intermetallic particles using fluorescence microscopy. It was found that oxygen reduction on the cathodic phases mainly supports active dissolution of nearby anodic intermetallic particles (e.g., *S*-phase (Al_2CuMg) particles). However, the reduction reaction also causes certain anodic dissolution in the adjacent matrix of cathodic phases as a side effect. The net current at the cathodic sites (the particle region and its trenched periphery) is cathodic.

The propensity to promote trenching in matrix is not the same for Al−Cu particles and Al−Cu−Fe−Mn particles although they are both cathodic to aluminium matrix [13]. Al−Cu particles are more susceptible to trenching than Al−Cu−Fe−Mn particles, especially in solutions of low chloride content [18]. OSORIO et al [19−21] reported the surface corrosion behavior of hypoeutectic Al−Cu cast alloys which are constituted by Al−Cu−Fe−Mn and θ-phase (Al_2Cu) particles. Reduction rate is about 4.5 times higher for the θ-phase region which exhibits a cathodic behavior with respect to the Al−Cu−Fe−Mn region. The alloy damage is achieved by θ-phase induced corrosion. A higher susceptibility to corrosion in NaCl solution is detected as the θ-phase fraction increases.

S-phase particle actively undergoes severe magnesium dealloying, which leads to the formation of high potential copper-rich remnant. Some of the remnant particles remained largely intact and others decomposed into clusters of 10−100 nm copper particles. Then, the clusters became detached from the alloy surface and were dispersed by mechanical action of growing corrosion product or solution movement. This observation suggests that nonfaradaic liberation of copper from corroding alloy surface is possible [22]. Copper enrichment of Al_2Cu and Al−Cu−Fe−Mn such as Al_7Cu_2Fe has also been highlighted by some authors [23,24]. When exposed to NaCl solution, these particles transform into a nanometric sponge of pure copper due to a selective dissolution, covered with amorphous aluminium hydroxide. The dealloying mechanism for various intermetallic phases depends both on copper content in the phase and crystallographic structure. Generally, aluminium dissolution is activated in the presence of magnesium and inhibited in the presence of iron.

ZHU and OOIJ [25] reported that *S*-phase particles were dealloyed of both magnesium and aluminium and the phenomenon was the most severe during the first 3.5 h of immersion in a neutral 0.6 mol/L NaCl solution, whereas the very interesting work of BOAG et al [26] demonstrated that the dealloying process was quickly completed within 5 min. Thus, even the same kind of intermetallic particles can be completely different in terms of kinetics. LACROIX et al [27,28] have performed statistical studies on the corrosion behavior of *S*-phase particles which show huge differences in their corrosion activity. When a particle dissolves it enriches with copper, which causes the increase in potential. In the case of non-corroded *S*-phase particles, almost no potential difference with the matrix was observed, suggesting the initial presence of a thick aluminium-rich oxide layer on the whole alloy. Most likely differences in the thickness of the aluminium-rich oxide layer will determine the corrosion performance. Difference in the electrochemical activity of the θ-phase particles was also detected and it was verified that these differences in activity determined the propagation of filiform corrosion underneath coatings [29].

S-phase particles play an important role in the corrosion of AA2024-T3 aluminium alloy [10,22,25, 26,30]. According to BLANC et al [30], the electrochemical behaviour of the alloy is similar to that of *S*-phase in the anodic range during electrochemical polarization in the presence of chloride ions. LEBLANC and FRANKEL [10] found that pitting of AA2024-T3 aluminium alloy originated at *S*-phase particles during corrosion testing in NaCl solutions under open-circuit condition. *S*-phase particles corroded even in the absence of local cathodic intermetallic particles such as Al−Cu−Fe−Mn particles.

BOAG et al [26] reported the end result of the dealloying process that trenching is developed around the copper-rich remnant of *S*-phase particles, indicating that these sites act as active cathodes. In fact, at a more advanced stage of degradation, *S*-phase particles were completely enveloped by a dark layer of reacted matrix adjacent to them [31]. However, attack around the isolated *S*-phase particles remains localized without spreading deeply into the matrix [26].

The aim of the current study is to advance the understanding of localized dissolution phenomenon related to intermetallic particles, including dealloying of *S*-phase particles and trenching in the periphery of *S*-phase particles and Al−Cu−Fe−Mn−(Si) particles. Corrosion behaviours of clustered *S*-phase and θ-phase particles were also investigated using a combination of electron microscopy and ultramicrotomy. Experimental proof of microgalvanic coupling on metallurgical scale and the relationship between the metallurgy and the electrochemical properties were characterized in order to

provide input data for microscale corrosion models of Al−Cu−Mg alloys.

2 Experimental

Cold-rolled sheet AA2024-T3 aluminium alloy with thickness of 1.6 mm (4.45% Cu, 0.28% Fe, 1.34% Mg, 0.54% Mn, 0.065% Si, 0.14% Zn, 15×10^{-6} Ni, 120×10^{-6} V and 20×10^{-6} Zr, Al Bal., mass fraction) was used in this work. Specimens with dimensions of 20 mm × 20 mm × 1.6 mm, were mechanically ground with 800, 1200 and 4000 grit silicon carbide paper and polished sequentially using 6, 3 and 1 μm diamond paste with water-free polishing liquid as lubricant, and then cleaned ultrasonically in an acetone bath and dried in a cool air stream.

Electrochemical measurement was carried out by polarizing the specimen in positive direction from 0.1 V minus to open circuit potential (OCP) to potentials in anodic region at the rate of 1 mV/s. Saturated calomel reference electrode (SCE), platinum counter electrode, and specimen were connected to a Solartron 1090 electrochemical measuring unit with input impedance of 1×10^{9} Ω, which was interfaced to a personal computer via a two-terminal cell connection. Potential and current were recorded using Coreware software which produced graphical output of the changing potential and current density over the time period of the experiment.

Immersion testing was carried out in 3.5% (mass fraction) NaCl (analytical grade) solution and deionized water open to air from a few minutes to 24 h. Specimens before and after immersion testing were examined using an FEI QUANTA 600 scanning electron microscope (SEM) equipped with energy dispersive X-ray (EDX) facilities. For secondary electron (SE) and backscattered electron (BSE) imaging the accelerating voltage of 15 kV was employed. NanoScope III MultiMode AFM was used to determine the topography of the AA2024-T3 aluminium alloy. A silicon cantilever, 125 μm in length, with a spring constant of 0.12 N/m and a resonant frequency of 242−396 kHz, was utilized. The scanning rates were adjusted to values between 0.5 to 1 Hz according to the scanned area and surface morphology.

The alloy sheet was also cut to dimensions of 20 mm × 7 mm × 1.6 mm and subsequently trimmed to a sharp tip with a glass knife exposing a cutting area of about 200 μm × 50 μm in order to generate ultra-microtomed specimens. After a series of cutting at a step size of 15 nm, thin electron-transparent sections of the alloy were spread and immersed in deionized water, and then collected onto 38 μm nickel grids. The thin sections were then examined using a JOEL 2000 FXII transmission electron microscope (TEM) operated at 300 kV.

3 Results and discussion

3.1 Dealloying of *S*-phase particles

Three intermetallic phases were identified in the AA2024-T3 aluminium alloy. They are *S*-phase that is rich in aluminium, copper and magnesium, θ-phase that is rich in aluminium and copper only, and α-phase that is rich in aluminium, copper, iron and manganese with or without small amount of silicon. Figure 1 shows the SEM images of mechanically polished AA2024-T3 aluminium alloy before and after immersion in 3.5% NaCl solution for 15 min. Two intermetallic particles were present in the images but surface activities were mainly associated with particle A. The particle maintained its shape after immersion but with reduced size. As indicated in the micrograph, its dimension w reduced from 5.1 to 4.7 μm. Cracks were formed in the particle, likely due to dehydration of corrosion product after the specimen was dried. Also, trenching is evident around the particle except for the top region.

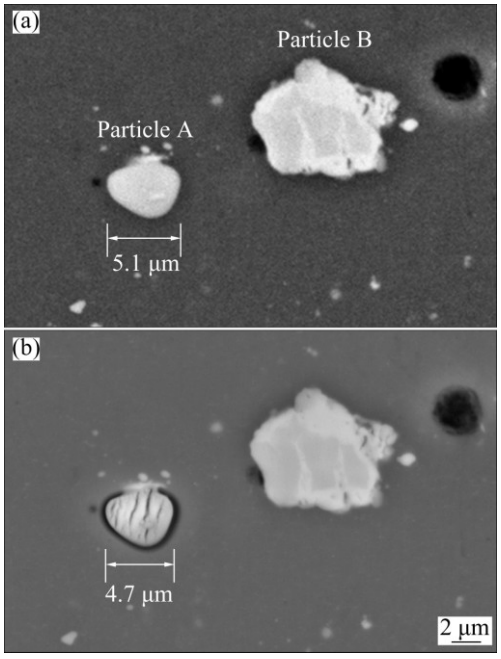

Fig. 1 SEM images of AA2024-T3 aluminium alloy: (a) Before immersion; (b) After immersion in 3.5% NaCl solution for 15 min, revealing dealloyed *S*-phase particle and intact Al−Cu−Fe−Mn−(Si) particle

EDX analysis was conducted at the central position of the active particle before immersion, as listed in Table 1. It has a chemical composition of 75.2% Al, 12.9% Cu, 10.3% Mg and 1.6% O. The mole ratio should be 2:1:1 for Al/Cu/Mg in *S*-phase. Since the mole ratio of Cu to Mg is 1:1 roughly, it was believed that some aluminium signal was detected from the surrounding aluminium matrix due to the electron beam−specimen

interaction volume. Thus, despite the increased aluminium, the intermetallic particle is identified as an *S*-phase particle. EDX analysis was conducted at exactly the same position of the particle after immersion. Clearly, there is profound decrease in magnesium content with relatively constant copper content, indicating that the particle was depleted of magnesium during immersion. The content of aluminium decreased slightly from 75.2% to 71.9% (mole fraction), indicating that the particle was also dealloyed of aluminium. Corrosion product has deposited on the dealloyed intermetallic particle, leading to significant increase in oxygen content, from 1.6% to 14.7% (mole fraction).

Table 1 EDX analysis of single *S*-phase particle before and after immersion

Time/min	Mole fraction/%			
	Al	Cu	O	Mg
0	75.2±1.89	12.9±0.89	1.6±0.12	10.3±1.00
15	71.9±1.76	11.6±0.93	14.7±1.04	1.8±0.15

The surface morphology of the aluminium alloy after immersion was characterized by AFM. Two-dimensional (2D) topographic maps are shown in Figs. 2(a) and (b). The brightness scale is illustrated on the right of the maps, indicating that brighter regions are higher than darker regions. Three-dimensional (3D) maps of the area are displayed in Figs. 2(c) and (d). From both 2D and 3D maps, trenching is evident around the *S*-phase particle shown in Fig. 2(b). The particle in Fig. 2(a) induced only half-trenching, indicating that development of the trench was not uniform in the particle's periphery.

Freshly generated foils of AA2024-T3 aluminium alloy were immersed in deionized water for 1 min before TEM examination. Figure 3(a) shows TEM image of one of such thin foils, illustrating a partially dissolved *S*-phase particle. The nano-scale particle-like structure of the dealloyed *S*-phase particle is displayed at increased magnification in Fig. 3(c). The size of the nano-scale particle ranges from 5 to 20 nm. Selected area diffraction of the dealloyed region in *S*-phase particle is shown in Fig. 3(b). The diffraction pattern is made up of discontinuous arch rings, indicating a polycrystalline structure of the *S*-phase particle remnant. By measuring the distance from the centre of diffraction pattern to the rings, *d*-spacing can be calculated. They are all consistent with *d*-spacing values in body-centred cubic (BCC) copper, indicating that *S*-phase transformed into pure copper phase after dealloying of aluminium and magnesium. Attack in aluminium matrix is also revealed with cellular texture forming close to the intermetallic particle. The cells in the texture become smaller as

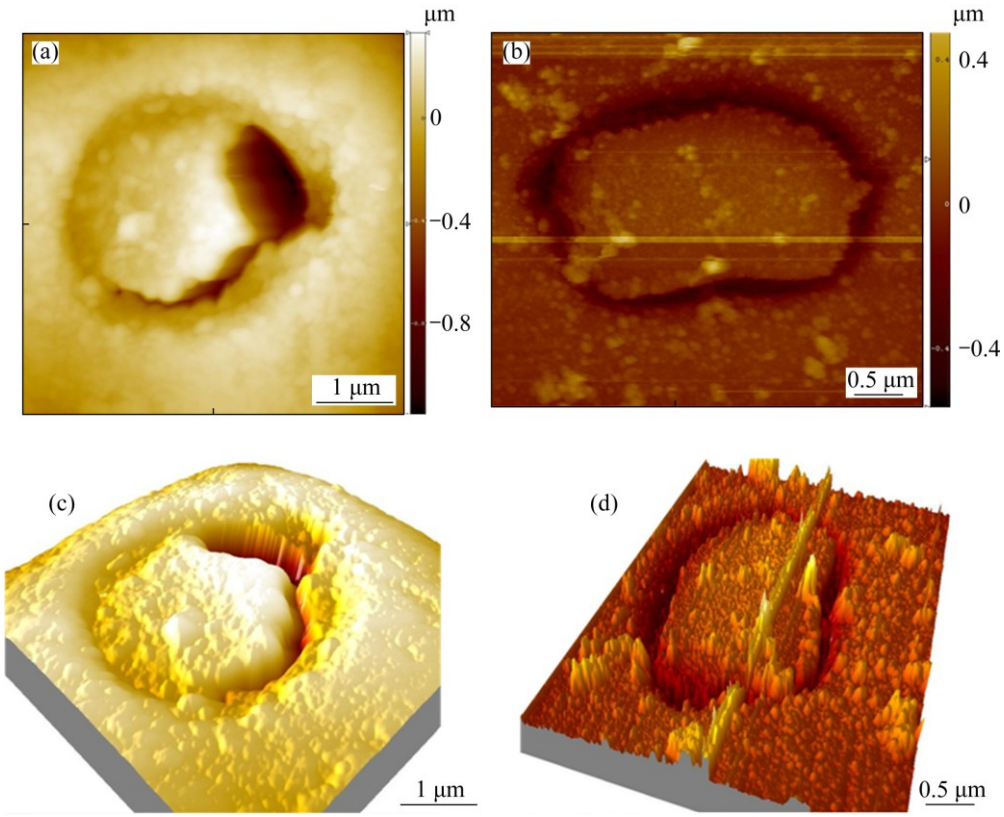

Fig. 2 AFM images of AA2024-T3 aluminium alloy after immersion in 3.5% NaCl solution for 1 h and 3.5 h, respectively, revealing half-circle and whole-circle trenching at *S*-phase particle: (a, b) 2D image; (c, d) 3D image

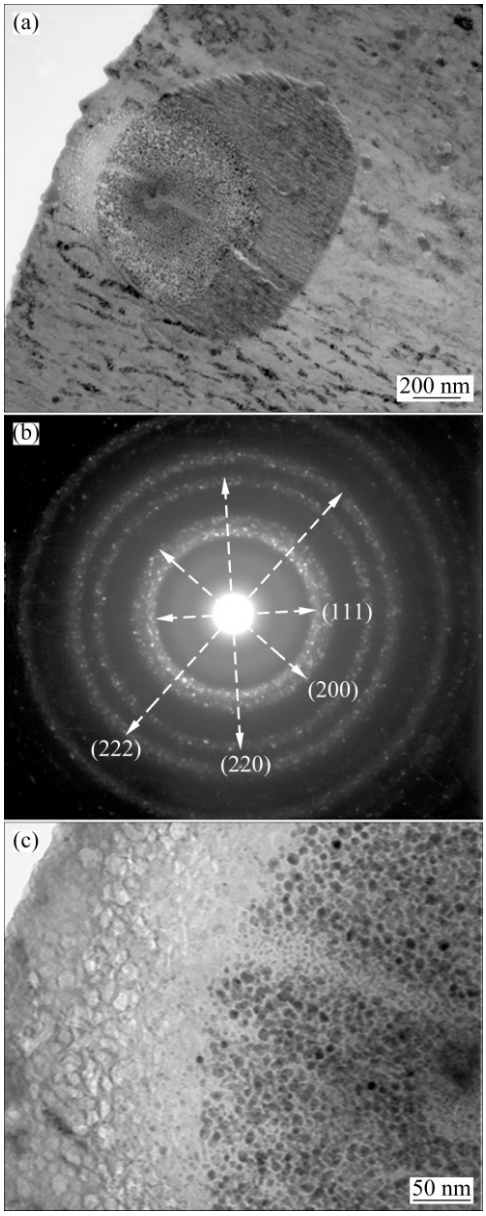

Fig. 3 TEM images of ultramicrotomed foil of AA2024-T3 aluminium alloy after immersion in deionized water for 1 min, revealing dealloyed *S*-phase particle: (a) General view; (b) Diffraction pattern of dealloyed part of *S*-phase particle; (c) At increased magnification

located farther away from the particle and finally disappear. Apparently, attack in the intermetallic particle and matrix is more severe on one side of the particle.

The OCP−time response of the Al−Cu−Mg alloy in 3.5% NaCl solution is displayed in Fig. 4(a), with the value stabilized at around −0.60 V (vs SCE). Figure 4(b) shows the potential−current density curve of electrochemical polarization of the alloy from 0.1 V minus to OCP to 0.5 V above breakdown potential, exhibiting an anodic current plateau. Correspondingly, the current density value increased slowly from 1×10^{-6} to 1×10^{-4} mA/cm^2 before the breakdown potential.

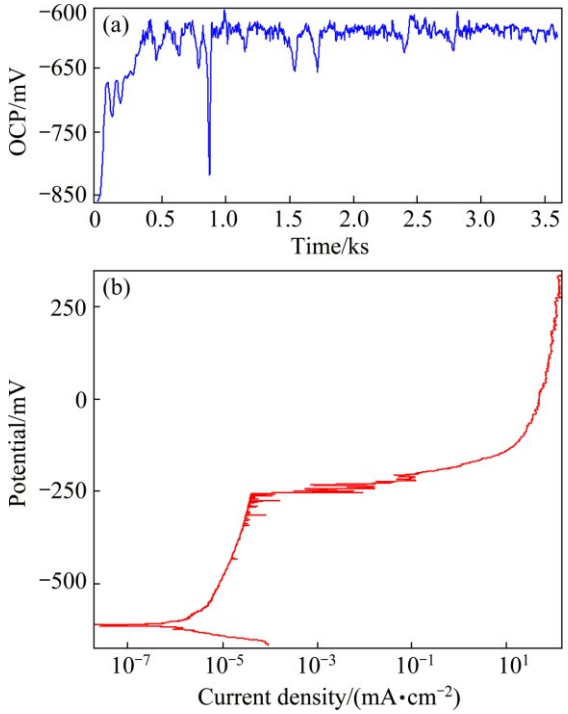

Fig. 4 OCP−time curve (a) and potential−current density curve (b) of electrochemical polarization of AA2024-T3 aluminium alloy in 3.5% NaCl solution

The OCP of *S*-phase in NaCl solution [11,32] is more negative than that for the alloy, consequently, these particles are anodically active at the OCP of AA2024-T3 aluminium alloy and undergo dissolution. Trenching in the periphery of the particles has been reported [10,22,25,26] most likely due to the switching of the *S*-phase from an anodic attack site to a cathode after the particle is enriched with copper [33]. For example, the OCP of copper at around −300 mV (vs SCE) is much more positive than that for AA2024-T3 aluminium alloy. And there are various reports for the OCP of θ-phase in NaCl solution from around −0.53 (vs SCE) [11,32] to −0.67 V (vs SCE) [34] which spans the OCP of the alloy. The remnant therefore tends to have a more positive OCP than the alloy. Thus, the dealloyed *S*-phase particles support cathodic reactions, leading to anodic corrosion of the adjacent aluminium matrix.

Further, transmission electron image of Fig. 3(a) shows that, with only one third of the *S*-phase particle dealloyed, attack was already formed in the periphery of the particle. This indicates that aluminium matrix started to trench at the early stage of dealloying of the *S*-phase particle. The process was much earlier than that the particle was completely converted to a local cathode.

3.2 Trenching around single Al−Cu−Fe−Mn−(Si) particle

On the contrary to activities associated with *S*-phase particle, little change is observed on the Al−Cu−Fe−Mn−

(Si) particle after corrosion testing in 3.5% NaCl solution for 15 min (Fig. 1(b)), suggesting relatively inert nature of Al−Cu−Fe−Mn−(Si) phase. Corrosion behaviour associated with further Al−Cu−Fe−Mn−(Si) particles is shown in Fig. 5 (24 h immersion in NaCl solution). Three coarse intermetallic particles are present in the examined region. Trenching is found around the lower part of particle 1 and upper part of particle 2. The upper part of particle 1, the lower part of particle 2 and particle 3 are intact, indicating localized corrosion occurred in different places at different time. Such phenomenon can be explained as follows. Aluminium lost electrons during anodic dissolution of the matrix. Meanwhile, aluminium oxide is formed by oxygen diffusion through flaws in the oxide film [35]. Flaws are introduced in the periphery of intermetallic particles during mechanical polishing due to the difference between intermetallic phase and matrix in mechanical properties. Certain locations, where more flaws are present, become preferential sites for anodic dissolution.

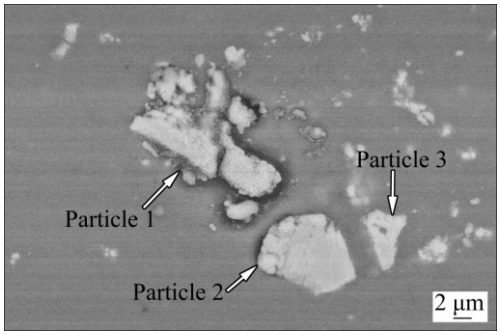

Fig. 5 SEM image of AA2024-T3 aluminium alloy after immersion in 3.5% NaCl solution for 24 h (BSE image, revealing trenching around Al−Cu−Fe−Mn−(Si) particles)

Figures 6(a) shows the scanning electron image of the AA2024-T3 aluminium alloy after immersion in 3.5% NaCl solution for 72 h. Corrosion of aluminium matrix is evident in the surrounding region of an Al−Cu−Fe−Mn−(Si) particle, forming a trench. This is consistent with the results in Fig. 5. Cross-section of the corrosion site was further examined at 45° tilting, as shown in Fig. 6(b). The sectioning direction and position are indicated by line *A*−*B* in Fig. 6(a). It is evident that corrosion is restricted in the shallow near-surface region of aluminium matrix.

Al−Cu−Fe−Mn−(Si) particle is expected to serve as local cathode since copper, iron and manganese all have a more positive electrode potential with respect to aluminium [10−13]. The OCPs of some Al−Cu−Fe−Mn−(Si) particles are provided in Tables 2 and 3, e.g., −0.55 mV for Al_7Cu_2Fe, −0.54 to −0.56 mV for Al_3Fe. As a consequence, if a micro electrochemical cell could be formed at Al−Cu−Fe−Mn−(Si) particles, aluminium matrix in the surrounding region should work as local anode. Due to the limited area of local cathode to support oxygen reduction, anodic dissolution of the surrounding material proceeds slowly. This explains the fact that has been observed: trenching in the periphery of an Al−Cu−Fe−Mn−(Si) particle took relatively long time to initiate.

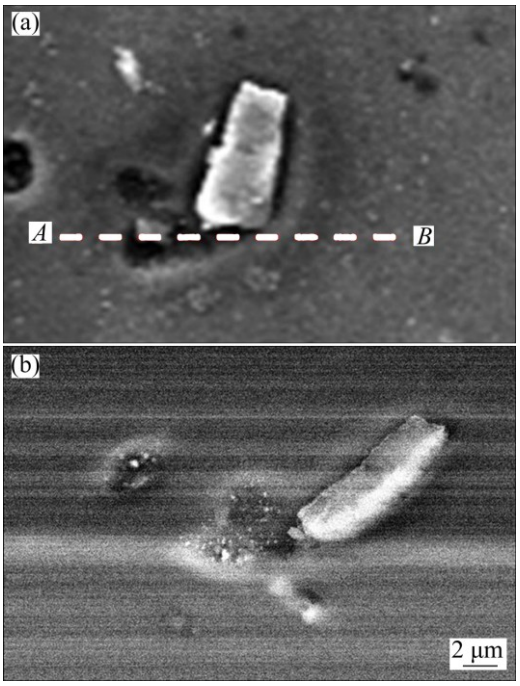

Fig. 6 SEM images of Al−Cu−Fe−Mn−(Si) particle after immersion in 3.5% NaCl solution for 72 h: (a) SE image; (b) BSE image with 45° tilting

Further, according to the results of SZKLARSKA-SMIALOWSKA [36,37], the product of current density and pit diameter (*Jr*) should be higher than 1×10^{-2} A/cm to sustain the aggressive solution (low pH) in a stably growing pit (or trench). Restricted anodic corrosion of aluminium matrix may fail to provide sufficient current density in the periphery of Al−Cu−Fe−Mn−(Si) particles. Thus, as shown in Fig. 6(b), localized attack is restricted in the shallow near-surface region at Al−Cu−Fe−Mn−(Si) particles during immersion of the alloy in NaCl solution.

3.3 Corrosion behaviour of clustered *S*-phase and *θ*-phase particles

Figure 7 shows an optical micrograph of AA2024-T3 aluminium alloy after immersion in 3.5% NaCl solution for 40 min. A number of single particles are displayed on the left of the image, exhibiting localized attack. A cluster of coarse intermetallic particles, around 30 μm in diameter, are evident on the right of the image. Interestingly, localized corrosion occurred on part of the cluster. The rest of the cluster shows little evidence of attack.

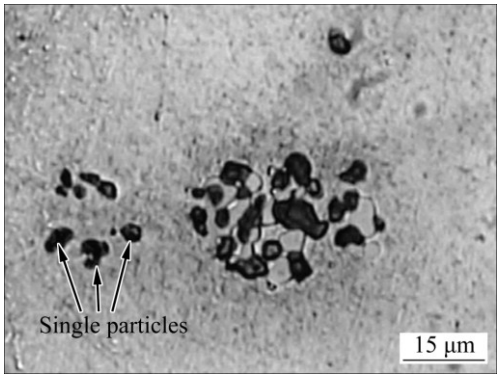

Fig. 7 OM image of AA2024-T3 aluminium alloy after immersion in 3.5% NaCl for 40 min, revealing corrosion at cluster of intermetallic particles

SEM image and EDX spectra of the alloy after immersion in 3.5% NaCl solution for 4 h are shown in Fig. 8, revealing a further cluster of intermetallic particles. EDX analysis was carried out on the cluster and its periphery. Again, it is evident that localized corrosion is associated with a portion of the particles. These particles exhibit a porous structure. Spectrum 1 from one of these particles (Position 1) exhibits peaks of oxygen and copper, indicating that they are *S*-phase particles dealloyed of magnesium and aluminium. Trenching is also revealed in the periphery of dealloyed *S*-phase particles. This is the same as the corrosion behaviour of single *S*-phase particles, suggesting consistent corrosion mechanism. Spectrum 2 from the matrix (Position 2) exhibits peaks of oxygen and aluminium, indicating that the matrix is covered with corrosion product. Other particles in the cluster and their periphery matrix exhibit little evidence of corrosion. Spectrum 3 from one of these particles (Position 3) shows peaks of oxygen, copper and aluminium, indicating that they are aluminium- and copper-containing θ-phase. It is suggested that they have relatively inert nature with respect to *S*-phase particles.

Localized corrosion associated with clustered *S*-phase and θ-phase particles was also examined by TEM. Thin foil of AA2024-T3 aluminium alloy was immersed in deionized water for 1 min. An area including a cluster of *S*-phase and θ-phase particles is displayed in Fig. 9(a). Corrosion occurred on a number of locations within the cluster and at the interface of intermetallic and aluminium matrix. One of the corrosion sites, framed in Fig. 9(a), is illustrated at increased magnification in Fig. 9(b). It is clearly revealed that the circular corroded area is mainly located within the *S*-phase particle, but extending into the surrounding aluminium matrix. The inner region of the corroded area exhibits a porous structure comprised of nano-scale particles. The morphology is similar to that shown in Fig. 3 of the single *S*-phase particle after selective dissolution of magnesium and aluminium. The outer region of the corroded area exhibits a texture structure, indicating dissolution of aluminium matrix.

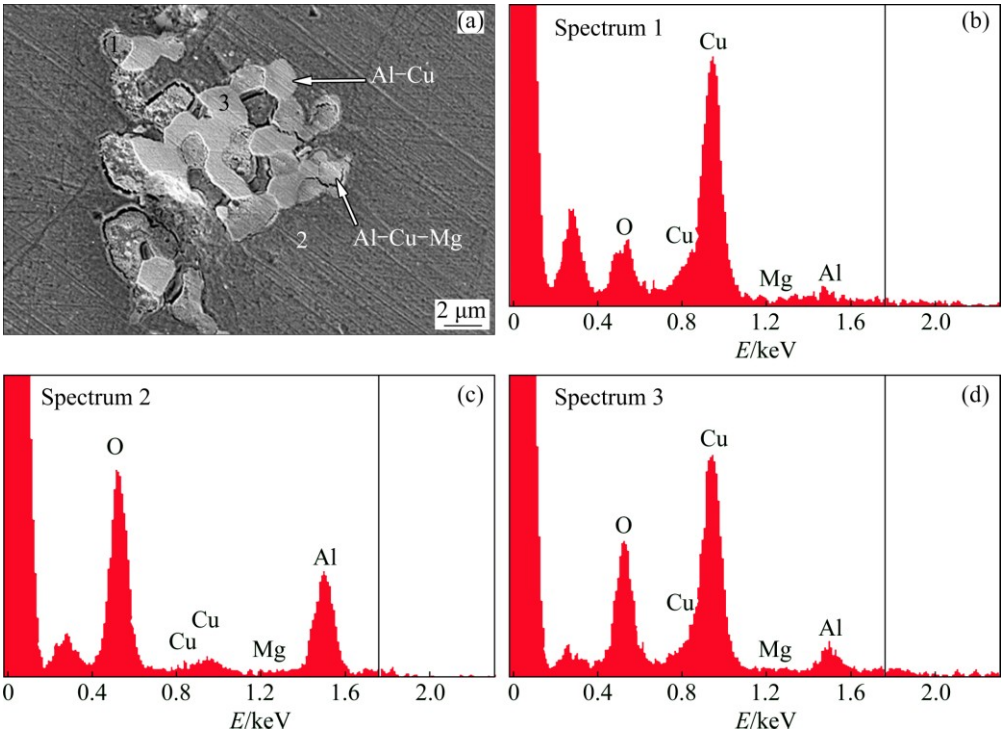

Fig. 8 SEM image (a) and EDX spectra (b−d) of AA2024-T3 aluminium alloy after immersion in 3.5% NaCl for 4 h, indicating preferential dissolution of *S*-phase particles in cluster of *S*-phase and θ-phase particles

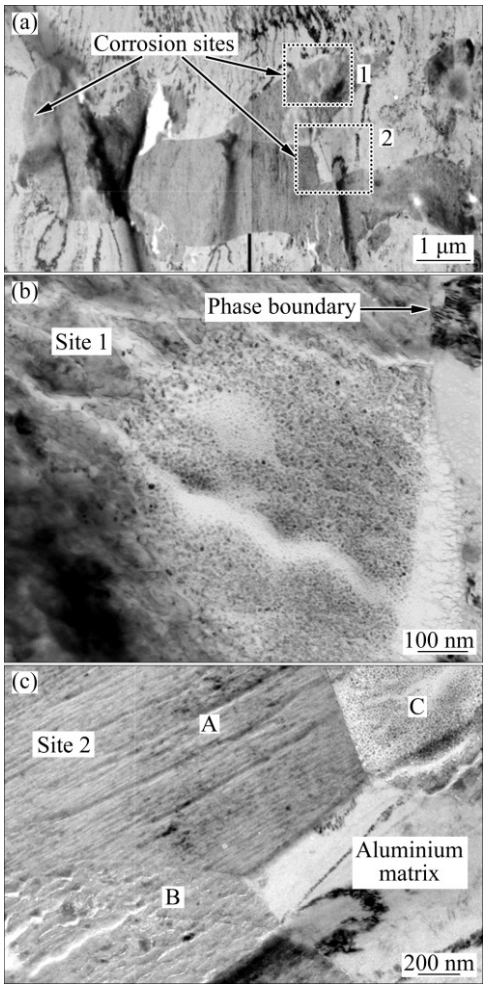

Fig. 9 TEM images of ultramicrotomed foil of AA2024-T3 aluminium alloy after immersion in deionized water for 1 min, revealing preferential corrosion of *S*-phase particles in cluster of *S*-phase and *θ*-phase particles: (a) At low magnification; (b, c) At increased magnification

Corrosion site 2 is displayed in Fig. 9(c). Three particles (labelled as A, B and C) and aluminium matrix are evident. The corroded region in particle C (*S*-phase) exhibits a porous structure comprised of nano particles. Interestingly, unlike the circular shape of dealloyed regions found in Figs. 3 and 9(b), the round boundary of the porous structure here is interrupted by the interface between particle A (*θ*-phase) and particle C. Dealloying is well restricted within particle C, with little development into the neighbouring particle A. From the low magnification image of Fig. 9(a), little morphological change is observed on the *θ*-phase particle, indicating high corrosion-resistance.

The presence of *S*-phase particles on the alloy surface alters the local properties of oxide film [33], providing favourable sites for the chloride to penetrate through the film and to initiate corrosion on the alloy surface. The formation of air-formed oxide film on *θ*-phase particles leads to the development of a copper-rich thin layer, 2−4 nm in thickness, at the particle/film interface, therefore, leading to modification of the electrochemical properties of the alloys [38].

The values of OCP for intermetallic phases are sensitive to experimental conditions. Electrochemical data obtained on synthetic phases for the intermetallic particles in aluminium alloys are listed in Table 2 [39]. In Table 3, a summary of measurement was performed by BIRBILIS and BUCHHEIT [11] using a micro capillary electrochemical cell. Corrosion potential of *S*-phase is in the general vicinity of −0.88 to −1.00 V (vs SCE) in 0.1 mol/L NaCl solution. The other two electrode potentials in the micro electrochemical cell existing at a cluster of *S*-phase and *θ*-phase particles are −0.69 V (vs SCE) of aluminium matrix (equivalent to Al−4%Cu supersaturated solid solution) and −0.53 to −0.67 V (vs SCE) of *θ*-phase. The largest difference in electrochemical potential is between *S*-phase and *θ*-phase. Thus, *θ*-phase provides the main driving force for *S*-phase dealloying.

Table 2 Electrode potentials of aluminium solid solutions and intermetallic phases with respect to 0.1 mol/L calomel electrode in aqueous solutions of 53 g/L NaCl and 3 g/L H_2O_2 at 25 °C [39]

Aluminium solid solution or intermetallic phase	Potential/V
Al_2CuMg	−1.00
Al (99.95%)	−0.85
Al−2%Cu supersaturated solid solution	−0.75
Al−4%Cu supersaturated solid solution	−0.69
Al_3Fe	−0.56
Al_2Cu	−0.53

Table 3 Electrochemical data as function of pH for intermetallic phases [11]

Stoichiometry	pH	φ_{corr}(vs SCE)/mV
Al_2CuMg	2.5	−750
	6	−883
	10	−850
Al_2Cu	2.5	−546
	6	−665
	10	−739
Al_7Cu_2Fe	2.5	−535
	6	−551
	10	−604
Al_3Fe	2.5	−510
	6	−539
	10	−408

Further, only very short distance is present between the two phases within a cluster of *S*-phase and *θ*-phase particles. Solution resistance between the two phases is at its smallest value. This also contributes to the possibility of *θ*-phase particle serving as local cathode. Otherwise, if the solution resistance within the electrochemical circuit is significant, current density is reduced, which means that the dissolution rate of *S*-phase is reduced. Thus, clusters of *S*-phase and *θ*-phase particles are preferential sites for localized corrosion to initiate.

4 Conclusions

1) The dealloyed *S*-phase particles exhibited porous, polycrystalline structure comprised of body-centred cubic copper particles with sizes of 5−20 nm.

2) Aluminium matrix started to trench in the periphery of *S*-phase particles at the early stage of dealloying.

3) The development of trenching in Al−Cu−Fe−Mn−(Si) particle's periphery was not uniform and took longer time to initiate than *S*-phase dealloying.

4) The localized corrosion at a cluster of *S*-phase and *θ*-phase particles was mainly associated with *S*-phase particles. *θ*-phase particles and their periphery matrix were intact, indicating their relatively inert nature with respect to *S*-phase. The cluster was preferential site for localized corrosion to initiate due to large electrochemical potential difference between *S*-phase and *θ*-phase particles.

References

[1] LAUDISE R A C. Aging of U.S. air force aircraft [R]. National Research Council (United States), Report No.: NMAB-488-2. Washington: National Academy Press, 1997.

[2] ANONYMOU S. Success stories: air force: material substitution and new sealing technologies keep airframes flying longer [J]. AMPTIAC Quarterly, 2009, 7: 57−61.

[3] HATCH J E. Aluminium: Properties and physical metallurgy [M]. Ohio: ASM International, 1984.

[4] HAHN G T, ROSENFIELD A R. Metallurgical factors affecting fracture toughness of aluminum-alloys [J]. Metallurgical and Materials Transactions A, 1975, 6: 653−668.

[5] HUGHES A E, MACRAE C, WILSON N, TORPY A, MUSTER T H, GLENN A M. Sheet AA2024-T3: A new investigation of microstructure and composition [J]. Surface and Interface Analysis, 2010, 42: 334−338.

[6] HUGHES A E, GLENN A M, WILSON N, MOFFATT A, MORTON A J, BUCHHEIT R G. A consistent description of intermetallic particle composition: An analysis of ten batches of AA2024-T3 [J]. Surface and Interface Analysis, 2013, 45: 1558−1563.

[7] THOMPSON G E, HASHIMOTO T, ZHONG X L, CURIONI M, ZHOU X, SKELDON P, WITHERS P J, CARRA J A, MONTEITH A G. Revealing the three dimensional internal structure of aluminium alloys [J]. Surface and Interface Analysis, 2013, 45: 1536−1542.

[8] DEROSE J A, SUTER T, BALKOWIEC A, MICHALSKI J, KURZYDLOWSKI K J, SCHMUTZ P. Localised corrosion initiation and microstructural characterisation of an Al 2024 alloy with a higher Cu to Mg ratio [J]. Corrosion Science, 2012, 55: 313−325.

[9] ZHOU X, LUO C, HASHIMOTO T, HUGHES A E, THOMPSON G E. Study of localized corrosion in AA2024 aluminium alloy using electron tomography [J]. Corrosion Science, 2012, 58: 299−306.

[10] LEBLANC P, FRANKEL G S. A study of corrosion and pitting initiation of AA2024-T3 using atomic force microscopy [J]. Journal of the Electrochemical Society B, 2002, 149: 239−247.

[11] BIRBILIS N, BUCHHEIT R G. Investigation and discussion of characteristics for intermetallic phases common to aluminum alloys as a function of solution pH [J]. Journal of the Electrochemical Society, 2008, 155: 1−4.

[12] BUCHLER M, WATARI T, SMYRL W H. Investigation of the initiation of localized corrosion on aluminum alloys by using fluorescence microscopy [J]. Corrosion Science, 2000, 42: 1661−1668.

[13] SCHNEIDER O, ILEVBARE G O, SCULLY J R, KELLY R G. In situ confocal laser scanning microscopy of AA2024-T3 corrosion metrology. II: Trench formation around particles [J]. Journal of the Electrochemical Society B, 2004, 151: 453−464.

[14] JIANG H W, YE L Y, ZHANG X M, GU G, ZHANG P, WU Y L. Intermetallic phase evolution of 5059 aluminum alloy during homogenization [J]. Transactions of Nonferrous Metals Society of China, 2013, 23: 3553−3560.

[15] ZHENG Y L, LI C B, LIU S D, DENG Y L, ZHANG X M. Effect of homogenization time on quench sensitivity of 7085 aluminum alloy [J]. Transactions of Nonferrous Metals Society of China, 2014, 24: 2275−2281.

[16] CONG F G, ZHAO G, JIANG F, TIAN N, LI R E. Effect of homogenization treatment on microstructure and mechanical properties of DC cast 7X50 aluminum alloy [J]. Transactions of Nonferrous Metals Society of China, 2015, 25: 1027−1034.

[17] WANG B, CHEN X H, PAN F S, MAO J J, FANG Y. Effects of cold rolling and heat treatment on microstructure and mechanical properties of AA 5052 aluminum alloy [J]. Transactions of Nonferrous Metals Society of China, 2015, 25: 2481−2489.

[18] LIU Y, ZHANG X M, ZHANG H. Role of secondary phase particles of 2519A aluminium alloy in localised corrosion [J]. Materials Research Innovations, 2014, 17(S): s83−s88.

[19] OSORIO W R, SPINELLI J E, FREIRE C M A, BALLESTER M C, GARCIA A. The roles of Al_2Cu and dendritic refinement on surface corrosion resistance of hypoeutectic Al−Cu alloys immersed in H_2SO_4 [J]. Journal of Alloys and Compounds, 2007, 443: 87−93.

[20] OSORIO W R, PEIXOTO L C, GARCIA L R, GARCIA A. Corrosion behavior of hypoeutectic Al−Cu alloys in H_2SO_4 and NaCl solutions [J]. Acta Metallurgica Sinica, 2009, 22: 241−246.

[21] OSORIO W R, MOUTINHO D J, PEIXOTO L C, GARCIA A. Macrosegregation and microstructure dendritic array affecting the electrochemical behaviour of ternary Al−Cu−Si alloys [J]. Electrochimica Acta, 2011, 56: 8412−8421.

[22] HASHIMOTO T, CURIONI M, ZHOU X, MANCUSO J, SKELDON P, THOMPSON G E. Investigation of dealloying by ultra-high-resolution nanotomography [J]. Surface and Interface Analysis, 2013, 45: 1548−1552.

[23] ROCCA E, TARDELLI J, MATHIEU S. On the galvanic coupling of bulk-AlCu intermetallic phases (Al_2Cu, Al_7Cu_2Fe) and pure aluminium in NaCl Solution [J]. ECS Meeting Abstracts, 2014, 3: 755.

[24] LEBOUIL S, TARDELLI J, ROCCA E, VOLOVITCH P, OGLE K. Dealloying of Al_2Cu, Al_7Cu_2Fe and Al_2CuMg intermetallic phases to form nanoparticulate cooper films [J]. Materials and Corrosion, 2014, 65: 416−424.

[25] ZHU D, van OOIJ W J. Corrosion protection of AA 2024-T3 by bis-[3-(triethoxysilyl)propyl]tetrasulfide in neutral sodium chloride solution. Part 1: Corrosion of AA2024-T3 [J]. Corrosion Science, 2003, 45: 2163−2175.
[26] BOAG A, HUGHES A E, GLENN A M, MUSTER T H, MCCULLOCH D. Corrosion of AA2024-T3. Part I: Localised corrosion of isolated IM particles [J]. Corrosion Science, 2011, 53: 17−26.
[27] LACROIX L, RESSIER L, BLANC C, MANKOWSKI G. Statistical study of the corrosion behavior of Al_2CuMg intermetallics in AA2024-T351 by SKPFM [J]. Journal of the Electrochemical Society, 2008, 155: 395−396.
[28] LACROIX L, RESSIER L, BLANC C, MANKOWSKI G. Combination of AFM, SKPFM, and SIMS to study the corrosion behavior of *S*-phase particles in AA2024-T351 [J]. Journal of the Electrochemical Society, 2008, 155: C131−C137.
[29] SENOZ C, BORODIN S, STRATMANN M, ROHWERDER M. In situ detection of differences in the electrochemical activity of Al_2Cu IMPs and investigation of their effect on FFC by scanning Kelvin probe force microscopy [J]. Corrosion Science, 2012, 58: 307−314.
[30] BLANC C, FREULON A, LAFONT M C, KIHN Y, MANKOWSKI G. Modelling the corrosion behaviour of Al_2CuMg coarse particles in copper-rich aluminium alloys [J]. Corrosion Science, 2006, 48: 3838−3851.
[31] KING P C, COLE I S, CORRIGAN P A, HUGHES A E, MUSTER T H. FIB/SEM study of AA2024 corrosion under a seawater drop: Part I [J]. Corrosion Science, 2011, 53: 1086−1096.
[32] BOAG A, TAYLOR R J, MUSTER T H, GOODMAN N, MCCULLOCH D, RYAN C, ROUT B, JAMIESON D, HUGHES A E. Stable pit formation on AA2024-T3 in a NaCl environment [J]. Corrosion Science, 2010, 52: 90−103.
[33] LACROIX L, BLANC C, PEBERE N, THOMPSON G E, TRIBOLLET B, VIVIER V. Simulating the galvanic coupling between S-Al_2CuMg phase particles and the matrix of 2024 aerospace aluminium alloy [J]. Corrosion Science, 2012, 64: 213−221.
[34] BIRBILIS N, BUCHHEIT R G. Electrochemical characteristics of intermetallic phases in aluminum alloys: An experimental survey and discussion [J]. Journal of the Electrochemistry Society B, 2005, 152: 140−151.
[35] MCCAFFERTY E. Sequence of steps in the pitting of aluminum by chloride ions [J]. Corrosion Science, 2003, 45: 1421−1438.
[36] SZKLARSKA-SMIALOWSKA Z. Insight into the pitting corrosion behavior of aluminum alloys [J]. Corrosion Science, 1992, 33: 1193−1202.
[37] SZKLARSKA-SMIALOWSKA Z. Pitting corrosion of aluminum [J]. Corrosion Science, 1999, 41: 1743−1767.
[38] ZHOU X, THOMPSON G E, HABAZAKI H, SHIMIZU K, SKELDON P, WOOD G C. Copper enrichment in Al-Cu alloys due to electropolishing and anodic oxidation [J]. Thin Solid Films, 1997, 293: 327−332.
[39] DAVIS J R. ASM metals handbook (Volume 1) [M]. Cleveland: American Society for Metals, 1961.

Al−Cu−Mg 合金在氯化钠溶液浸泡过程中萌生于单个和簇状金属间化合物粒子的局部溶解

骆 晨[1]，Xiaorong ZHOU[2]，George E. THOMPSON[2]

1. 中航工业北京航空材料研究院 航空材料先进腐蚀与防护航空科技重点实验室，北京 100095；
2. School of Materials, The University of Manchester, Manchester M13 9PL, UK

摘 要：为了深刻理解 AA2024-T3 铝合金暴露在含氯水介质中金属间化合物相的响应方式，运用扫描电镜获得腐蚀试验前后合金表面的形貌信息，进行能谱分析确定金属间化合物粒子的成分变化，使用原子力显微镜检测金属间化合物相电化学反应所引起的高度变化，并对去合金金化的 Al_2CuMg 粒子及其周边区域进行透射电镜分析。研究发现，去合金化 Al_2CuMg 粒子为由 5~20 nm 大小的体心立方铜粒子组成的多孔多晶体结构；在去合金化早期，铝基体就开始在 Al_2CuMg 粒子周边出现沟槽状腐蚀；Al−Cu−Fe−Mn−(Si)粒子周边沟槽状腐蚀的发展不均匀且比 Al_2CuMg 去合金化需要更长时间萌生；由 Al_2CuMg 和 Al_2Cu 组成的粒子簇的局部腐蚀主要与 Al_2CuMg 粒子相关。

关键词：铝合金；金属间化合物粒子；局部溶解；去合金化；沟槽状腐蚀

(Edited by Wei-ping CHEN)